Femtosecond Microscopy of Surface Plasmon Polariton Wave Packet Evolution at the Silver/Vacuum Interface

3 AUTHORS, INCLUDING:

Niko Pontius
Helmholtz-Zentrum Berlin
59 PUBLICATIONS **1,206** CITATIONS

Hrvoje Petek
University of Pittsburgh
217 PUBLICATIONS **5,374** CITATIONS

Femtosecond Microscopy of Surface Plasmon Polariton Wave Packet Evolution at the Silver/Vacuum Interface

Atsushi Kubo,[†,‡] Niko Pontius,[†,§] and Hrvoje Petek*,[†]

Department of Physics and Astronomy and Petersen Institute for NanoScience and Engineering, University of Pittsburgh, Pittsburgh, Pennsylvania 15260, and PRESTO, Japan Science and Technology Agency, 4-1-8 Honcho Kawaguchi, Saitama, Japan

ABSTRACT

A movie of the dispersive and dissipative propagation of surface plasmon polariton (SPP) wave packets at a silver/vacuum interface is recorded by the interferometric time-resolved photoemission electron microscopy with 60 nm spatial resolution and 330 as frame interval. The evolution of SPP wave packets is imaged through a two-path interference created by a pair of 10 fs phase correlated pump−probe light pulses at 400 nm. The wave packet evolution is simulated using the complex dielectric function of silver.

Surface plasmon polaritons (SPPs) are propagating electromagnetic modes of metal−dielectric interfaces. Limited by the ohmic losses in metals, SPP waves can propagate on micrometer to millimeter length scales.[1,2] The SPP propagation in metal strips,[3] waveguides,[4] and nanodot arrays[5,6] has been investigated as a means of transporting and processing optical signals in photonic devices and focusing of electromagnetic waves on the nanometer scale.

As the SPP wave vector increases, according to the dispersion function derived from the experimental dielectric constants of Ag (Figure 1a), the group velocity of SPP wave packets at the Ag/vacuum interface decreases from the speed of light in vacuum in the zero wave vector limit. In the optical region, which offers the largest bandwidths, the SPP dispersion and dissipation limit the propagation lengths and bandwidths of SPP wave packets.[7] Although the dielectric properties of noble metals in the infrared region are well-known, there have been few[3] quantitative studies of the SPP wave packet propagation in the strongly dispersive region, where the SPP frequency asymptotically approaches the surface plasmon resonance at 3.7 eV. In order to realize SPP wave applications at optical frequencies, the ability to image and characterize the SPP wave packet propagation is indispensable.

The electromagnetic wave transients can be characterized through measurements of their envelope and phase with the subwavelength spatial and suboptical cycle pump−probe delay resolution. Phase information can be obtained in all optical measurements only if the imaging light has much shorter wavelength than the probing light or by means of near-field optical techniques. The imaging of electromagnetic wave transients in solids has been limited to terahertz frequency phonon polaritons in ionic crystals[8] and slow light in photonic crystals,[9] which have substantially longer wavelengths, slower group velocities, and longer lifetimes than SPPs. Scanning near-field optical microscopy has been used to observe static interference patterns among scattered SPP waves,[10,11] as well as between SPP waves and external continuous wave excitation fields.[7,12,13] The ultrafast propagation of SPP wave packets has been deduced through heterodyne mixing of a scattered SPP field with an external reference beam.[14] However, the characterization of SPP wave packet propagation at visible and near-ultraviolet frequencies has not been achieved with purely optical techniques.

In this Letter, we report on the imaging of SPP waves with unprecedented <10 fs temporal and 60 nm spatial resolution using a hybrid technique that combines the time resolution of femtosecond laser spectroscopy with the suboptical wavelength imaging of photoelectrons with a photoemission electron microscope (PEEM).[15] An intense external field, which is both the source and the probe of the SPP wave packet, creates a standing polarization wave in an Ag film through two-path interference (Figure 1b).[12] The PEEM records a nonlinear map of this polarization grating with resolution that exceeds the SPP wavelength by imaging the spatial distribution of photoelectrons that are generated through two-photon photoemission (2PP).[16] By scanning the

* Corresponding author: petek@pitt.edu.
† Department of Physics and Astronomy and Petersen Institute for NanoScience and Engineering, University of Pittsburgh.
‡ PRESTO, Japan Science and Technology Agency.
§ Present address: BESSY mbH, Albert-Einstein Str. 15, 12489 Berlin, Germany.
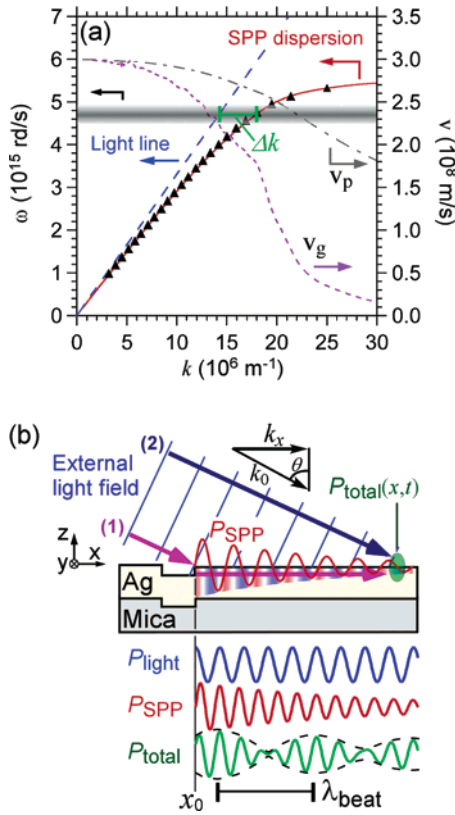
Figure 1. (a) The dispersion function of light incident at 65° angle (long dash) and SPP (solid line, used to simulate the PEEM images; triangles, from ref 18). The graded density horizontal line represents the frequency and the bandwidth of the excitation light. Δk is the momentum mismatch at the excitation frequency between light in vacuum and SPP. The group ($\nu_g = d\omega/dk$) and the phase velocities ($\nu_p = \omega/k$) of SPP also are shown. (b) Schematic of the experimental setup showing the two-path interference between P_{SPP} (path 1) and P_{light} (path 2) that is imaged in ITR-PEEM experiments. The damped sinusoidal line indicates the traverse component of the SPP wave, whose phase is delayed from the longitudinal component (red/white/blue striped pattern) by $\pi/2$. P_{total} is modulated by the interference between P_{SPP} and P_{light} with the beating length $\lambda_{beat} = 2\pi/\Delta k$. PEEM records the nonlinear image of the envelope of P_{total} shown by the dashed lines.

mutual delay τ_d between identical, phase-correlated pump and probe pulses in $^1/_4$ optical cycle steps and recording the resulting change in the polarization interference pattern, we create a movie of the SPP wave packet propagation at the Ag/vacuum interface. We describe a model for the PEEM imaging of the SPP wave packet evolution according to a modified complex dielectric function of Ag.

The apparatus for the interferometric time-resolved photoemission electron microscopy (ITR-PEEM) is described elsewhere.[15] The second harmonic of a self-made Ti:sapphire laser oscillator provides 10 fs excitation pulses at 400 nm with 90 MHz repetition rate and 100 mW average power. A Mach–Zehnder interferometer generates collinear phase-locked pump–probe pulse pairs with τ_d defined to ±25 as.[17] To record individual frames of an ITR-PEEM movie, the delay is incremented in intervals of $\Delta\tau_d = 330$ as corresponding to a change in the relative phase of $\pi/2$ ($^1/_4$ cycle) of the 400 nm carrier light. The p-polarized laser light incident at 65° from the surface normal is focused onto a

~100 × 200 μm spot on the sample at the focal plane of the PEEM (FOCUS GmbH). Because the energy of two photons (2 × $h\nu$ = 6.2 eV) is necessary to overcome the work function of the Ag sample (4.2 eV), the PEEM records a spatially inhomogeneous map of the 2PP yield, which is proportional to the nonlinear polarization P_{total}[4] impressed in the sample. Because 2PP signals are much stronger for TM than for TE excitation, we only consider the surface normal component of the induced polarization.[17] For each delay, PEEM movie images are integrated over many independent pump–probe cycles during the exposure time of 10 s. The surface topography of the sample is ascertained from a conventional, single photon PEEM image excited with an Hg lamp ($h\nu$ = 4.89 eV).

The sample is formed by depositing an 83 nm thick polycrystalline silver film onto a freshly cleaved mica substrate. The Ag film has a mirror finish disrupted by occasional line defects from cleaving. The sample is introduced into the PEEM chamber from air without further processing.

The momentum mismatch Δk between the incident light and the SPP wave packet, which is given by the horizontal distance between the light line and the SPP dispersion curve in Figure 1a, prevents the incoming 400 nm electromagnetic field from exciting SPP waves in a continuous Ag film. An additional source of momentum can be supplied by a discontinuity in the film with subwavelength dimensions. The external field excites an SPP wave packet at a step (origin x_0). The wave packet propagates from x_0 along path 1 in Figure 1b as a polarization wave ($P_{SPP}(x,t)$) at the vacuum/Ag interface. The same external field propagating through vacuum along path 2 interacts with the continuous Ag film to create an additional source of local polarization $P_{light} = \epsilon_0\chi E_{light}$. Because of the phase velocity mismatch, the relative phase between the SPP wave and the component of the external field projected onto the sample surface depends on x beyond x_0. The total polarization excited in the film ($P_{total} = P_{SPP} + P_{light}$) is modulated with a period $\lambda_{beat} = 2\pi/\Delta k = 1.7 \mu$m, along the Ag film surface through the interference between the component waves excited by *single* pulses. In addition to this static polarization grating, when exciting the sample with phase correlated light pulse pairs, there is a dynamic, τ_d dependent, component of the grating corresponding to the interference between the pump–pulse induced P_{SPP} and probe–pulse induced P_{light}. An ITR-PEEM movie images the SPP wave packet propagation through this τ_d dependent dynamic component of P_{total}.

Figure 2 shows a topographic PEEM image excited with the Hg lamp incident from the right side, and selected frames from an ITR-PEEM movie taken with femtosecond laser pump–probe pulses incident from the left side. The shadowing effect in the Hg lamp excited image (intensity drop, Figure 2, inset) indicates the presence of a groove defect formed by cleaving the mica substrate, on an otherwise optically flat surface. By contrast, the femtosecond laser-excited PEEM images in panels a–f in Figures 2 for $\Delta\tau_d$ intervals of 9.34 fs, corresponding to phase increments of 7 × 2π, show τ_d-dependent, damped oscillatory patterns
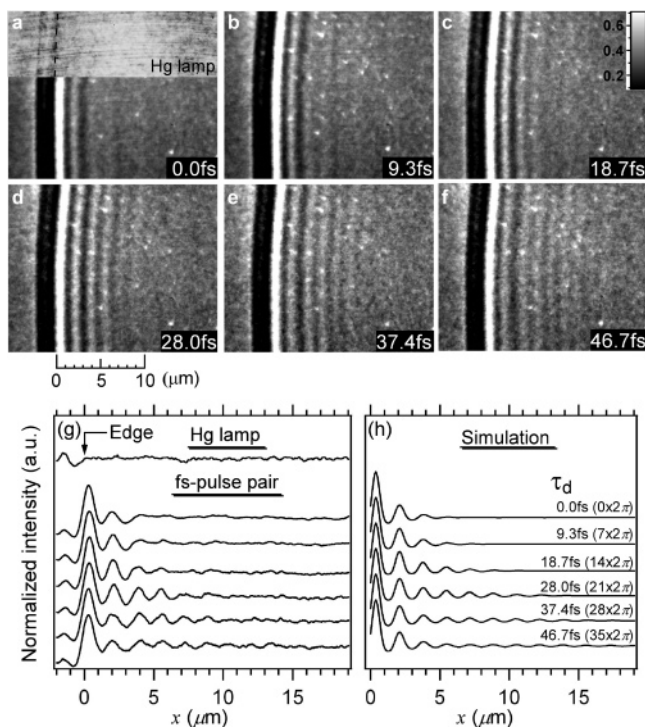
Figure 2. (a−f); ITR-PEEM movie frames of the silver film excited with phase-locked pump−probe pulse pairs. The delay time τ_d (phase) for each image is advanced from (a) 0.0 fs ($0 \times 2\pi$), to (f) 46.7 fs ($35 \times 2\pi$) in steps of 9.3 fs ($7 \times 2\pi$). Inset of (a) shows the Ag film topography measured with the Hg lamp excitation. The broken line locates the film discontinuity. (g) PEEM image intensity profiles of (a−f) and (h) their simulation for the corresponding τ_d. The complete ITR-PEEM movie taken with 330 as ($\pi/2$-phase) delay increments is available as Supporting Information.

starting from the rising (right) edge of the grove. Increasing τ_d from 0 ($0 \times 2\pi$) to 37.4 fs ($28 \times 2\pi$) causes the oscillatory interference pattern to extend further from x_0 (Figure 2a−e). For τ_d = 46.7 fs ($35 \times 2\pi$, Figure 2f) and beyond, τ_d exceeds substantially the SPP lifetime and the amplitude of the pump−probe induced interference is attenuated.

Before presenting a model for the SPP wave propagation and imaging, we describe some general features of the ITR-PEEM movie frames in Figure 2. Panels g and h of Figure 2 show cross sections of the oscillatory patterns in Figure 2a−f and their simulation, respectively. The observed wavelength of 1.7 ± 0.15 μm for the interference pattern corresponds well to the λ_{beat} associated with Δk in Figure 1. The SPP and light fields propagate along the surface with their corresponding wave vectors ($k_{SPP} = 17.9 \times 10^6$ m^{-1} and $k_x = k_0 \sin \theta = 14.2 \times 10^6$ m^{-1}). The constructive interference between them occurs whenever the SPP and surface projected fields propagate by approximately 5 and 4 wavelengths (λ_{SPP} = 352 nm; $\lambda_x = 2\pi/k_x = 441$ nm), respectively. The extent of the oscillatory pattern from the origin reflects the distance the pump excited SPP wave packet has traveled when it is overtaken by the probe light.

On the basis of this interpretation, we simulate the PEEM images to extract the underlying SPP wave packet dynamics. The 2PP intensity at position x proportional to $P_{total}(x,t)^4$ is integrated over the pump−probe pulse excitation cycle:

$$I_{PEEM}(x) = \int_{-\infty}^{+\infty} (P_{total}(x,t))^4 \, dt \quad (1)$$

Since the excitation geometry defines P_{light} within a randomly evolving phase (Figure 1b), our main task is to develop a model for P_{SPP} that reproduces the evolving interference pattern in the ITR-PEEM movie.

The SPP wave packet is generated by the external electric field, which drives charge density oscillations in the Ag film at the subwavelength discontinuity located at x_0. The external field couples into the longitudinal component of SPP, which is phase shifted by $\pi/2$ from its transverse component. Because only the transverse component of $P_{SPP}(x,t)$ can interfere with P_{light}, this phase shift defines the position of interference maxima and minima in the PEEM images. The propagation of the wave packet $P_{SPP}(x,t)$ for $x > 0$ is governed by the complex dielectric function of Ag. Figure 1a shows that at 400 nm the group velocity v_g of the wave packet is substantially slower than its phase velocity v_p. As the wave packet propagates it broadens and attenuates through dispersion and dephasing.

We calculate the evolution of the SPP wave packet by propagating its individual Fourier components. An SPP wave packet excited at x_0 by the transform-limited Gaussian pulse of 10 fs duration is analyzed into its complex Fourier components, $P_{SPP}(x_0,t) = \sum_i r_i \exp(i(\omega_i t + \phi_i))$, where r_i and ϕ_i represent the amplitude and initial phase of a component wave with the angular frequency ω_i. From x_0, the component waves propagate with phase velocity $v_p(\omega_i) = \omega_i/k_{SPP}'(\omega_i)$ and attenuate with a characteristic length $\kappa(\omega_i) = 1/2k_{SPP}''(w_i)$, which are given by the real and imaginary parts of the complex SPP wave vector, $k_{SPP}(\omega_i) = k_{SPP}'(\omega_i) + ik_{SPP}''(\omega_i)$, respectively. The propagated wave packet $P_{SPP}(x,t)$ is then synthesized from its Fourier components $P_{SPP}(x,t) = \sum_i r_i' \exp(i(\omega_i t + \phi_i'))$, where the amplitude and the accumulated phase are given by $r_i' = r_i \exp(-k_{SPP}''(\omega_i)x)$ and $\phi_i' = \phi_i + k_{SPP}'(\omega_i)x$, respectively.

The complex SPP wave vector is connected to the dielectric function of Ag, $\epsilon = \epsilon' + i\epsilon''$, through $k_{SPP} = (\omega/c)(\epsilon/1 + \epsilon)^{1/2}$. For $\lambda > 340$ nm, the condition $\epsilon'' < |\epsilon'|$ is satisfied, and the real and imaginary parts of k_{SPP} can be approximated by $k_{SPP}' = (\omega/c)(\epsilon'/(1 + \epsilon))^{1/2}$ and $k_{SPP}'' = (\omega/c)(\epsilon'/(1 + \epsilon'))^{3/2}(\epsilon''/2\epsilon'^2)$, respectively.[18]

We adjusted $k_{SPP}'(\omega)$ and $k_{SPP}''(\omega)$ to obtain good agreement with the experimental ITR-PEEM movie images. The $k_{SPP}'(\omega)$ dispersion curve used for the simulation in Figure 1a agrees well with the values calculated from the dielectric constants for Ag of Johnson and Christy.[19] However, near 400 nm there is substantial uncertainty in the dielectric function of Ag. According to the optical constants of Johnson and Christy[19] and Palik,[20] the SPP propagation length κ at 400 nm is calculated to be 4.0 and 0.8 μm, respectively. Our derived value of $\kappa = 3.0$ μm, which falls within this range, gives an SPP lifetime of κ/v_p = 12 fs.

Though the ITR-PEEM movie images show only the envelope of the interference pattern of P_{SPP} and P_{light}, we can deduce more details of the transient spatiotemporal evolution of the polarization fields through their simulation.
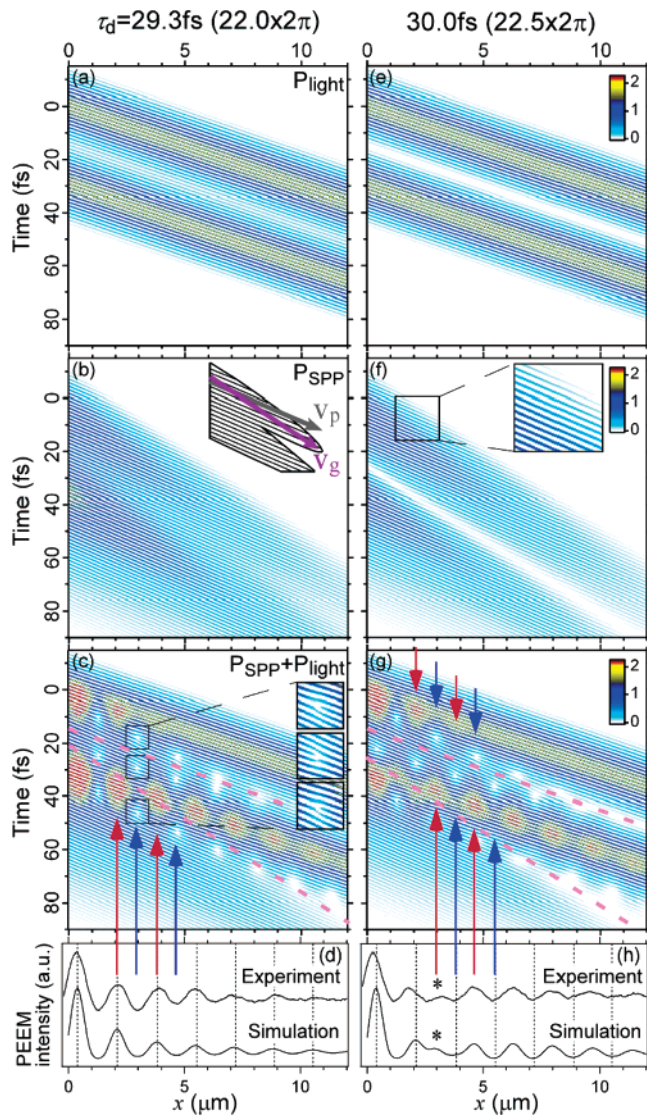
Figure 3. The calculated trajectories for P_{light} (a and e), P_{SPP} (b and f), and their sum, P_{total} (c and g), which are used to simulate the experimental PEEM image profiles in (d) and (h), respectively, for pump−probe delays corresponding to phase of $22.0 \times 2\pi$ and $22.5 \times 2\pi$ cycles of the carrier frequency. Only positive values of the sinusoidal polarization oscillations are plotted. The color scale indicates the polarization amplitude. Insets: (b) the direction of ν_p and ν_g for P_{SPP}; (f) an expanded image of the individual oscillations of P_{SPP}; (c) an expanded image of the self- (upper, lower) and pump−probe (middle) destructive interferences. The dashed lines in (c) and (g) delimit space−time regions where the polarization grating is dominated by the self-interference (upper and lower) and the pump−probe interference (middle). The red and blue arrows indicate the constructive and destructive interferences. The asterisk (*) in (h) indicates the phase-slip separating the spatial region dominated by the self-interference from the pump−probe interference. A high-resolution figure is available as Supporting Information.

Figure 3 presents a false color plot of the calculated amplitude of the polarization waves, $P_{light}(x,t)$, $P_{SPP}(x,t)$, and $P_{total}(x,t)$ employed in the simulation of ITR-PEEM images, for the in-phase ($22.0 \times 2\pi$, Figure 3a−c) and out-of-phase ($22.5 \times 2\pi$, Figure 3e−g) excitation. The polarization amplitude is plotted with respect to the spatial and temporal coordinates from the SPP origin. The parallel stripes of equal phase (Figure 3f inset) define individual oscillations of the

polarization fields. Profiles of the plots along the time and space axes give the evolution of fields in time at a given x and in space at a given t, respectively. The stripe intervals along the time and space axes give, respectively, the period (1.33 fs) and wavelengths λ_x (Figure 3a,e) and λ_{SPP} (Figure 3b,f) of the surface projected fields.

The plots of P_{light} in parts a and e of Figure 3 represent the space−time trajectories of the pump and probe fields: The individual pulses are separated by the delay time τ_d, and lines of equal phase have the slope of $1/\nu_p = \sin\theta/c$. While the pump and probe fields are connected without interruption of the phase for the in-phase excitation (Figure 3a), they exhibit destructive interference for the out-of-phase excitation (Figure 3e).

The plots of P_{SPP} in parts b and f of Figure 3 show the dispersive and dissipative propagation of SPP wave packets. The SPP packets excited at $x = 0$ by the pump−probe pulse sequences evolve in the lower-right direction of the spatiotemporal plots. The slope of the lines of equal phase corresponds to $1/\nu_p$. By contrast, the trajectory of the wave packet envelope is given by $1/\nu_g$ (Figure 3b inset). Because the SPP propagation occurs in the regime of normal dispersion (Figure 1a), ν_g is smaller than ν_p and the initially transform-limited SPP wave packet spreads as it propagates. The pump and probe excited SPP wave packets interfere constructively or destructively in the region of overlap depending on the mutual phase delay.

The plots of P_{total} in parts c and g of Figure 3 show the polarization grating formed by the superimposition P_{SPP} and P_{light} propagating from the same origin along paths 1 and 2 (Figure 1b), respectively. The mismatch between the phase velocities of P_{SPP} and P_{light} is responsible for the progressions of constructive and destructive interferences seen as sequences of amplitude minima (blue arrows) and maxima (red arrows) with a periodicity of 1.7 μm. This periodicity can be immediately recognized as $\lambda_{beat} = 2\pi/\Delta k$.

We separate the spatiotemporal plots for P_{total} into three regions bounded by broken lines in parts c and g of Figure 3, where different components of the interaction dominate. The P_{total} in the top and bottom regions is dominated by the *self-interference* of individual light pulses with their own SPP wave packets. In these regions, both the phase and the envelope of SPP wave packets follow their source light pulses because their ν_p and ν_g are both slower than that of the light. The interference patterns within these regions are independent of τ_d and occur even for single pulse excitation. The middle region is dominated by the interference between the P_{SPP} of the pump pulse with the P_{light} of the probe pulse (pump−probe interference). In this region, the P_{SPP} of the pump pulse is created first and is overtaken by P_{light} of the probe pulse on a time scale that depends on their relative group velocities and the pump−probe delay.

These two space and time interference pathways give the distinct spatiotemporal evolution of P_{total} in parts c and g of Figure 3. For instance, Figure 3c insets show magnified plots of the P_{total} fringes at the intensity minima caused by the destructive interference between P_{SPP} and P_{light}. The intensity minima occur when fringes of P_{total} undergo a π-phase shift.
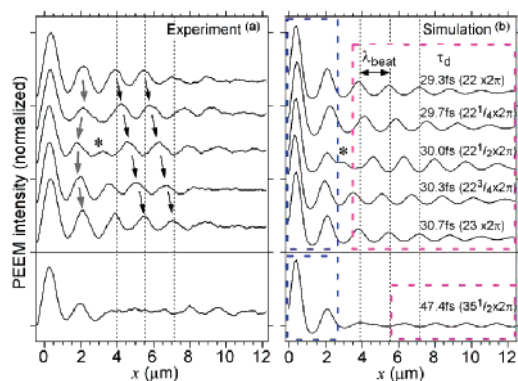
Figure 4. (a) Sequential cross sections of individual frames of the ITR-PEEM movie for the delay range of $(22-23) \times 2\pi$ phase and at $35.5 \times 2\pi$ phase and (b) their simulation for the corresponding τ_d. The blue and red rectangles indicate the self- and the pump−probe interference regions, respectively.

The sign of the phase shift is opposite in the self- and the pump−probe interference regions, depending on whether P_{SPP} is following or leading P_{light}.

The spatial location of the intensity extrema of P_{total}, i.e., the position of the polarization grating relative to x_0, is determined by the initial phase difference between P_{SPP} and P_{light} and the delay τ_d. For the self-interference regions, the location of the extrema is determined by the $\pi/2$ phase shift between P_{SPP} and P_{light} at x_0, and therefore, it is identical and delay independent. However, for the pump−probe region, advancing the pump−probe delay by 2π moves the extrema by λ_{beat}. The motion of the interference pattern is evident in the polarization grating for the out-of-phase excitation (Figure 3g), where the extrema in the pump−probe region are shifted by $\lambda_{beat}/2$ with respect to those of the self-interference regions or the in-phase excitation (Figure 3c).

To simulate the ITR-PEEM images, $P_{total}{}^4$ in eq 1 is integrated over the interaction time (single pump−probe cycle). Since the integration is performed along the time axis for each point on the x axis, the information on the individual field fringes is lost, and the experiment measures only the time integrated spatial polarization grating. For the in-phase excitation, the three interference progressions occur at the same distance from the origin and, therefore, add in-phase to give the maxima and minima in Figure 3d. However, for the out-of-phase excitation, the $\lambda_{beat}/2$ shift between the self- and pump−probe interferences gives rise to the corresponding phase slip in the 2PP intensity profile in Figure 3h (indicated by asterisks). Before the phase slip ($x < *$), the dominant contribution to PEEM images is the static self-interference, and past ($x > *$), it is the propagating pump−probe interference. Therefore, the τ_d-dependent SPP dynamics are revealed through the movement of PEEM images for $x > *$.

Figure 4 shows sequential cross sections of individual frames of the ITR-PEEM movie for the delay range corresponding to phase of $(22.0-23.0) \times 2\pi$ in the increments of $\pi/2$, and for the phase of $35.5 \times 2\pi$. The interference pattern for $x < *$ just oscillates back and forth in space because of a small contribution from the pump−probe interference to the total signal; however, for $x > *$ it

propagates to larger x as τ_d advances. The movement of SPP wave packet causes the polarization grating to propagate at the ν_g of SPP. At $35.5 \times 2\pi$ delay, we can distinguish the propagated SPP wave packet of the pump pulse from the self-interference region by a plateau that separates them. From the simulation, we determine $\nu_g = 1.83 \times 10^8$ m/s ($0.61c$) at 400 nm.

The ITR-PEEM technique combining the spatial and temporal resolution of electron microcopy and femtosecond laser spectroscopy offers a revolutionary method for imaging previously unobservable ultrafast dynamics of coherent fields and excited carriers in nanometer scale optical and electronic structures. Similar oscillatory interference patterns observed for other metals suggest that the SPP imaging method is not limited to Ag. The SPP wave packet imaging for the simplest case of a linear defect in a semi-infinite film holds promise for applying the ITR-PEEM to study of SPP dynamics in more complex structures that are under intense investigation for nanoplasmonic optics.

Supporting Information Available: The complete ITR-PEEM movie from which selected frames were presented in Figure 2 is available as qt and avi files and a high-resolution version of Figure 3 is available as a jpg file. This material is available free of charge via the Internet at http://pubs.acs.org.

References

(1) Barnes, W. L.; Dereux, A.; Ebbesen, T. W. *Nature* **2003**, *424*, 824−830.
(2) Berini, P.; Charbonneau, R.; Lahoud, N.; Mattiussi, G. *J. Appl. Phys.* **2005**, *98*, 043109.
(3) Lamprecht, B.; Krenn, J. R.; Schider, G.; Ditlbacher, H.; Salerno, M.; Felidj, N.; Leitner, A.; Aussenegg, F. R.; Weeber, J. C. *Appl. Phys. Lett.* **2001**, *79*, 51−53.
(4) Krenn, J. R.; Weeber, J.-C. *Philos. Trans. R. Soc. London, Ser. A* **2004**, *362*, 739−756.
(5) Maier, S. A.; Kik, P. G.; Atwater, H. A.; Meltzer, S.; Harel, E.; Koel, B. E.; Requicha, A. A. G. *Nat. Mater.* **2003**, *2*, 229−232.
(6) Nomura, W.; Ohtsu, M.; Yatsui, T. *Appl. Phys. Lett.* **2005**, *86*, 181108.
(7) Zayats, A. V.; Smolyaninov, I. I.; Maradudin, A. A. *Phys. Rep.* **2005**, *408*, 131−314.
(8) Feurer, T.; Vaughan, J. C.; Nelson, K. A. *Science* **2003**, *299*, 374−377.
(9) Gersen, H.; Karle, T. J.; Engelen, R. J. P.; Bogaerts, W.; Korterik, J. P.; van Hulst, N. F.; Krauss, T. F.; Kuipers, L. *Phys. Rev. Lett.* **2005**, *94*, 073903.
(10) Bozhevolnyi, S. I.; Pudonin, F. A. *Phys. Rev. Lett.* **1997**, *78*, 2823−2826.
(11) Hecht, B.; Bielefeldt, H.; Novotny, L.; Inouye, Y.; Polh, D. W. *Phys. Rev. Lett.* **1996**, *77*, 1889−1892.
(12) Salomon, L.; Bassou, G.; Aourag, H.; Dufour, J. P.; de Fornel, F.; Carcenac, F.; Zayats, A. V. *Phys. Rev. B* **2002**, *65*, 125409.
(13) Yin, L.; Vlasko-Vlasov, V. K.; Rydh, A.; Pearson, J.; Welp, U.; Chang, S.-H.; Gray, S. K.; Schatz, G. C.; Brown, D. B.; Kimball, C. W. *Appl. Phys. Lett.* **2004**, *85*, 467−469.

(14) Rokitski, R.; Tetz, K. A.; Fainman, Y. *Phys. Rev. Lett.* **2005**, *95*, 177401.

(15) Kubo, A.; Onda, K.; Petek, H.; Sun, Z.; Jung, Y. S.; Kim, H. K. *Nano Lett.* **2005**, *5*, 1123−1127.

(16) Cinchetti, M.; Gloskovskii, A.; Nepjiko, S. A.; Schönhense, G.; Rochholz, H.; Kreiter, M. *Phys. Rev. Lett.* **2005**, *95*, 047601.

(17) Petek, H.; Ogawa, S. *Prog. Surf. Sci.* **1997**, *56*, 239−310.

(18) Raether, H., *Surface Plasmons*; Springer: Berlin, 1988.

(19) Johnson, P. B.; Christy, R. W. *Phys. Rev. B* **1972**, *6*, 4370−4379.

(20) *Handbook of Optical Constants of Solids*; Palik, E. D., Ed.; Academic: New York, 1998.

NL0627846